Research Square

Preprints are preliminary reports that have not undergone peer review.
They should not be considered conclusive, used to inform clinical practice,
or referenced by the media as validated information.

Visible-light-activated $CdS/Ag_2S/g\text{-}C_3N_4$ nanozyme for sensitive colorimetric detection of CA19-9

Yan Cheng
First Hospital of Shanxi Medical University
Pengcheng Zhang
Shanxi Medical University
Shicheng Chen
Shanxi Medical University
Huiling Xue
Taiyuan University of Technology
Ying Zhan
Taiyuan University of Technology
Bing Zhang
zhangbing01@tyut.edu.cn

Taiyuan University of Technology

Research Article

Keywords: Colorimetric, Immunoassay, CA19-9, $CdS/Ag_2S/g\text{-}C_3N_4$, Visible light

Posted Date: July 27th, 2026

DOI: https://doi.org/10.21203/rs.3.rs-10221766/v1

License: This work is licensed under a Creative Commons Attribution 4.0 International License.
Read Full License

Additional Declarations: No competing interests reported.

Version of Record: A version of this preprint was published at Microchimica Acta on November 14th, 2026. See the published version at https://doi.org/10.1007/s00604-026-08539-w.

Abstract

Carbohydrate antigen 19 – 9 (CA19-9) serves as a pivotal serological indicator for pancreatic and gastrointestinal oncology. In this work, we engineered a sandwich-style colorimetric immunosensor employing a CdS/Ag_2S/g-C_3N_4 ternary heterojunction as a photo-responsive nanozyme label. Comprehensive physicochemical characterization including TEM, XRD, FTIR, and DRS confirmed the successful synthesis of the nanocomposite. Optical analysis revealed a narrowed bandgap of 2.25 eV, which facilitates broad visible-light harvesting and efficient suppression of photogenerated carrier recombination, thereby boosting catalytic kinetics. Mechanistic investigations identified photogenerated holes (h^+) as the primary oxidizing agents mediating the chromogenic reaction of 3,3',5,5'-tetramethylbenzidine (TMB). Under optimized assay conditions, the platform achieved a broad linear dynamic range of 2.5–45 U/mL and a low detection limit of 0.108 U/mL. Crucially, analysis of clinical serum specimens demonstrated high concordance with standard clinical methodologies, highlighting the sensor's robustness for early-stage tumor screening and point-of-care testing.

Introduction

Carbohydrate antigen 19 – 9 (CA19-9) stands as the most extensively utilized serological biomarker for pancreatic cancer and also exhibits elevated levels in several biliary, gastric, and colorectal malignancies [1–3]. In clinical practice, CA19-9 is routinely employed not only as an auxiliary diagnostic indicator but also for disease monitoring, therapeutic efficacy assessment, and recurrence surveillance. Nevertheless, its concentration in healthy individuals is generally extremely low (< 37 U mL^{-1}) [4], while early stage patients may display only slightly elevated levels. Moreover, non malignant conditions (e.g., cholestasis, pancreatitis) can lead to false positive elevations [5, 6]. Hence, developing new methods with high sensitivity, selective, and reliable quantification of CA19-9 in complex biological matrices is necessary.

Although established techniques such as ELISA and chemiluminescence immunoassays provide the sensitivity required for clinical CA19-9 detection [7–9], their dependence on thermolabile enzymes and costly, sophisticated equipment presents practical barriers. These limitations highlight the demand for streamlined alternatives that offer comparable specificity with simplified instrumentation and straightforward visual readouts. Colorimetric immunoassays fulfill this niche by converting target binding into visible color changes. This versatility allows for signal acquisition via direct observation, conventional microplate readers, or smartphone-based imaging, making them ideal for resource-limited settings [10–12].

- In colorimetric immunoassays, signal amplification labels are paramount for achieving high sensitivity without resorting to instrumental sophistication. While the conventional HRP/TMB system is well-established, its reliance on H_2O_2 and enzyme kinetics renders it vulnerable to fluctuations in pH, temperature, and endogenous inhibitors prevalent in biofluids [13, 14]. Photo-activated nanomaterials, particularly semiconductor heterojunctions, present a compelling alternative. By harnessing photons as an external stimulus, these catalysts bypass the need for

thermally labile biocatalysts and volatile peroxides, while their electronic band structures can be rationally engineered to promote charge separation and enhance surface redox kinetics [15, 16]. Graphitic carbon nitride (g-C_3N_4) is a prime candidate for such visible-light-harvesting scaffolds, owing to its metal-free composition, chemical robustness, and facile surface functionalization. However, pristine g-C_3N_4 suffers from a limited specific surface area and a high exciton binding energy, which precipitate rapid electron-hole recombination at the surface or within the bulk. This recombination severely curtails quantum efficiency and photocatalytic output. Consequently, strategic modifications—such as heterostructure fabrication, elemental doping, and defect engineering—are essential to mitigate these intrinsic limitations [17–20]. For example, Zhurenok et al. loaded Ni onto C_3N_4 to improve its photocatalytic performance [21]. Jiang et al. exploited a g-C_3N_4/ZnCdS/MoO_3 heterostructured photocatalyst, identifying a distinctive dual S-scheme charge transport mechanism as the origin of its efficient carrier separation [22].

In this study, a CdS/Ag_2S/g-C_3N_4 photocatalytic nanolabel was synthesized. By leveraging the energy level disparities among g-C_3N_4, CdS, and Ag_2S, an efficient Type-II heterojunction was established to separate electrons and holes. Both Ag_2S and CdS are narrow bandgap semiconductors, when integrated with g-C_3N_4, their absorption spectrum for visible light was significantly broadened. This synergistic effect extended the lifespan of photogenerated carriers, consequently generating a greater number of photogenerated holes (h^+), which is crucial for driving the oxidation coloration of TMB and achieving high sensitivity detection. A sandwich immunoassay was constructed based on CdS/Ag_2S/g-C_3N_4 nanomaterials, quantitative analysis and detection of CA19-9 were realized through the color reaction of TMB.

Experimental

Chemicals

CA19-9 antigen, mouse anti-CA19-9 monoclonal antibody (Ab) and bovine serum protein (BSA) were purchased from Sangon Biotech Co., Ltd (Shanghai, China); 1-(3-dimethylaminopropyl)-3-ethylcarbodiimide (EDC), carboxylated magnetic beads (-COOH, 5 mg mL^{-1}, 100–200 nm), 3,3',5,5'-tetramethylbenzidine (TMB), n-hydroxysuccinimide (NHS), melamine, thioacetamide (TAA), and silver nitrate ($AgNO_3$) were purchased from Aladdin Reagent Company (Shanghai, China). All other reagents are of analytical grade.

Synthesis of CdS/Ag_2S/g-C_3N_4 nanomaterials

The synthesis of carboxylated g-C_3N_4 was adapted from established literature protocols [23]. Initially, bulk g-C_3N_4 was derived from the thermal polycondensation of 10 g melamine precursor in an alumina crucible under a nitrogen stream. The furnace temperature was ramped to 380°C over 25 min, followed by a controlled ascent to 520°C (2°C min^{-1}), with a 4 h isothermal hold at the target temperature. The

resulting pale-yellow aggregate was pulverized into a fine powder. For surface functionalization, 1 g of this pristine g-C_3N_4 was subjected to reflux in 100 mL of 5 M HNO_3 for 24 h at 125°C. After cooling, the suspension underwent successive centrifugation and deionized water washes until a neutral pH was attained, followed by desiccation in a vacuum oven at 60°C to yield the carboxylated derivative.

The fabrication of the ternary CdS/Ag_2S/g-C_3N_4 heterojunction was achieved with modifications to a previously reported protocol [24]. Initially, 100 mg of carboxylated g-C_3N_4 was exfoliated in 20 mL of anhydrous ethanol via ultrasonication (30 min) to ensure a homogeneous dispersion. To this suspension, 161.5 µL of $AgNO_3$ (100 mM) was introduced dropwise under dark conditions, followed by magnetic stirring for 1 h to facilitate silver ion adsorption. Subsequently, 161.5 µL of thioacetamide (TAA, 50 mM) was added as a sulfur source, and the reaction proceeded in a 0°C ice bath with continuous stirring for 4 h. The resulting Ag_2S/g-C_3N_4 precipitate was harvested by centrifugation, washed, and desiccated in the dark. In the second step, 50 mg of this intermediate was re-dispersed in 100 mL of DI water and sonicated for 10 min. Following this, 6 mL of trisodium citrate (0.03 g mL^{-1}) was introduced as a capping agent under stirring. After 5 min, 10 mL of cadmium acetate (0.0145 g mL^{-1}) was added, and the pH was modulated to ~ 9.0 using ammonium hydroxide. Finally, 2.8 mL of thiourea (0.015 g mL^{-1}) was introduced, and the system was heated at 80°C for 3 h under oil bath conditions. The final nanocomposite CdS/Ag_2S/g-C_3N_4 was isolated via centrifugation, purified, and vacuum-dried.

Preparation of Ab labeled conjugates

The conventional carbodiimide coupling approach was utilized to fabricate antibody (Ab)-labeled magnetic beads [25]. Specifically, magnetic beads (MBs) at a concentration of 5 mg mL^{-1} were dissolved in a solution containing 100 mM 1-ethyl-3-(3-dimethylaminopropyl) carbodiimide (EDC) and 100 mM N-hydroxysuccinimide (NHS) at ambient temperature and activated through shaking for 30 min. Following magnetic separation, the beads were washed thrice with PBS buffer to eliminate excess EDC and NHS. Subsequently, 25 µL of Ab was introduced into the activated MB solution and incubated at 4°C overnight. After the reaction, the beads were washed again with PBS to remove unbound antibodies. The resultant Ab-labeled magnetic bead conjugates (designated as MB-Ab) were stored at 4°C for subsequent use. The Ab-CdS/Ag_2S/g-C_3N_4 nanoconjugates were synthesized using the same method and were stored in the refrigerator at 4°C.

Construction of the colorimetric immunosensor

Based on sandwich-type immunoassay format, a colorimetric sensing platform for the quantitative analysis of CA19-9 was devised (Scheme 1B). Concretely, 100 µL of MB-Ab conjugate was reacted with 25 µL of CA19-9 standards (variable concentrations) under orbital shaking at ambient temperature for 35 min. Following magnetic sequestration of the beads, the pellet was resuspended in 200 µL of PBS. Subsequently, 100 µL of Ab-functionalized CdS/Ag_2S/g-C_3N_4 nanoprobes (0.8 mg mL^{-1}) was introduced, and the mixture was incubated under identical conditions for another 35 min to assemble the ternary

immunocomplex (MB-Ab@CA19-9@Ab-CdS/Ag_2S/g-C_3N_4). After stringent magnetic washing cycles, the isolated complex was redispersed in 200 µL of ultrapure water. For signal transduction, 200 µL of acetate buffer (ABS, pH 4.0) and 400 µL of 7 mM TMB substrate were added sequentially. The enzymatic-mimicking reaction was activated by visible-light irradiation (λ ≥ 420 nm) from a xenon source for 8 min. Finally, the catalytic oxidation of TMB was monitored by recording the UV-vis absorption spectrum of the supernatant across the 350–700 nm range.

Preferred position of Scheme

Results and Discussion

Characterization of CdS/Ag_2S/g-C_3N_4 nanomaterials

Transmission electron microscopy (TEM) characterization reveals that the carboxylated g-C_3N_4 support possesses an ultrathin, crumpled lamellar morphology (Fig. 1A). Subsequent deposition of Ag_2S yields homogeneously anchored nanoparticles (~ 10 nm) across the g-C_3N_4 substrate (Fig. 1B). Further integration of CdS results in the loading of larger nanoparticles (~ 50 nm) onto the binary Ag_2S/g-C_3N_4 hybrid matrix (Fig. 1C). Powder X-ray diffraction (XRD) was utilized to scrutinize the crystalline phases of the as-synthesized CdS/Ag_2S/g-C_3N_4 composite (Fig. 1D). The prominent reflection at 27.3° is indexed to the characteristic (002) interplanar stacking of graphitic C_3N_4. Furthermore, distinct diffraction peaks located at 34.4°, 36.8°, and 43.4° corroborate the formation of orthorhombic Ag_2S, corresponding to the (− 121), (121), and (200) lattice planes, respectively. Additionally, peaks attributed to hexagonal CdS (JCPDS No. 41-1049) are evident at 24.82°, 26.36°, 43.84°, 47.52°, and 51.9°, matching the (100), (002), (110), (103), and (112) planes. The coexistence of these characteristic reflections unequivocally verifies the successful ternary heterostructure fabrication.

Fourier-transform infrared (FTIR) spectroscopy further elucidates the chemical integrity of the composite (Fig. 1E). The ternary CdS/Ag_2S/g-C_3N_4 spectrum preserves the characteristic vibrational fingerprints of the g-C_3N_4 backbone, implying that the carboxylation protocol does not perturb the intrinsic polymeric structure. Notably, the broad band attributed to N–H/O–H stretching undergoes a red-shift from 3431 cm^{-1} to approximately 3169 cm^{-1} and exhibits significant broadening. This spectral evolution is indicative of successful carboxyl functionalization, specifically corresponding to the C = O stretching vibrations of the introduced carboxylic acid groups. CdS and Ag_2S typically do not exhibit significant characteristic absorption peaks within the conventional FTIR measurement range. Furthermore, UV-vis diffuse reflectance spectroscopy (DRS) was utilized to probe the optical absorption characteristics of the composite (Fig. 1F). Relative to its monocomponent counterparts, the CdS/Ag_2S/g-C_3N_4 heterojunction exhibits a markedly enhanced visible-light-harvesting capability. Bandgap extrapolation reveals values of 2.79 eV for g-C_3N_4 and 2.42 eV for CdS, while the ternary composite displays a further red shift in light absorption, corresponding to a reduced bandgap of 2.25 eV, which substantiates its superior spectral responsiveness for visible-light-driven applications.

Preferred position of Fig.

Mechanism of the chromogenic system

To further validate the performance of the $CdS/Ag_2S/g\text{-}C_3N_4$ composite, experiments were carried out with TMB as the chromogenic substrate. As depicted in Fig. 2A, the absorbance at 370 nm of the $CdS/Ag_2S/g\text{-}C_3N_4$ system post illumination is stronger than that in the non illuminated state, which verifies the photocatalytic activity of $CdS/Ag_2S/g\text{-}C_3N_4$. Moreover, four chromogenic systems were established: $g\text{-}C_3N_4$, Ag_2S, CdS, and $CdS/Ag_2S/g\text{-}C_3N_4$ nanocomposites under identical conditions (100 μL of 0.5 mg mL^{-1} material + 100 μL deionized water + 400 μL 5 mM TMB + 200 μL 0.1 M ABS buffer at pH 4.0, illuminated for 8 min). The results in Fig. 2B indicate that all four systems yield blue solutions under visible light irradiation, with distinct characteristic absorption peaks at 370 nm and 652 nm. The absorbance of the $CdS/Ag_2S/g\text{-}C_3N_4$ nanocomposite system is notably higher than that of the other systems, suggesting its enhanced catalytic capacity in the photocatalytic chromogenic reaction. The observed enhancement is predominantly attributed to the construction of the ternary heterojunction, which facilitates the efficient spatial separation of photogenerated electron-hole pairs, thereby significantly boosting the redox capacity of the catalyst (Fig. 2C). To evaluate the efficiency of charge separation, PL spectra were recorded under 370 nm laser excitation (Fig. 2D). While $g\text{-}C_3N_4$ showed a strong characteristic emission at 434 nm (curve ‘a’), the $CdS/Ag_2S/g\text{-}C_3N_4$ composite exhibited a drastic quenching of this signal (curve ‘d’). This suppression confirms that the formation of the heterojunction acts as an efficient channel for separating photogenerated carriers, thereby reducing radiative decay.

A systematic investigation into the underlying mechanism of TMB oxidation catalyzed by the ternary $CdS/Ag_2S/g\text{-}C_3N_4$ nanocomposite was conducted via a series of rigorously designed control studies under visible-light exposure. In typical photocatalytic reactions, the active species that may be generated under visible light irradiation encompass hydroxyl radicals (·OH), singlet oxygen ($^1O_2$), superoxide anions ($\cdot O_2^-$), and photogenerated holes (h^+). To identify the primary reactive oxygen species (ROS) driving the chromogenic process, a radical trapping study was conducted using specific quenchers: 5 mM KBr (h^+ scavenger), 7.5 mg/mL tryptophan ($^1O_2$ quencher), 1 mM isopropanol (·OH scavenger), and 5 μM p-benzoquinone ($\cdot O_2^-$ scavenger). Samples without quenchers served as the control group. The results in Fig. 2E reveal that after the addition of isopropanol (curve ‘d’) and tryptophan (curve ‘c’), the solution color and its absorbance peak display almost no significant alteration, indicating that ·OH and $^1O_2$ have no influence on this reaction. After the addition of p-benzoquinone, only a slight reduction in absorbance is observed, implying that superoxide anions ($\cdot O_2^-$) may exist in the reaction but play a limited role (curve ‘b’). After the addition of KI, the absorbance decreases significantly (curve ‘e’), suggesting that photogenerated holes (h^+) are the principal active species driving the TMB oxidation reaction. Moreover, EPR detection was conducted using the radical trapping agent TEMPO (specific for h^+). As shown in Fig. 2F, the TEMPO signal decays rapidly under illumination, further validating the presence of h^+ as the main active species.

Preferred position of Fig. 2

Performance of colorimetric immunosensor

To guarantee optimal performance in subsequent experiments, the pH, antibody antigen incubation time, and TMB concentration were optimized. As depicted in Fig. 3A, the absorbance initially increases and subsequently decreases with the increasing pH, attaining a maximum at a pH of 4.0 in the ABS buffer. Based on Fig. 3B, when the antibody antigen binding time is 35 min, the absorbance reaches its maximum and then remains stable. From Fig. 3C, as the TMB concentration rises, the absorbance of the oxidized TMB solution first increases and then tends to stabilize. In conclusion, the optimal conditions for subsequent experiments are an ABS buffer pH of 4.0, an incubation time of 35 min, and a TMB concentration of 7 mM. Under the optimal experimental conditions, $CdS/Ag_2S/g\text{-}C_3N_4$ based colorimetric immunosensor was employed to detect a series of CA19-9 concentrations. As delineated in Fig. 3D, the absorbance intensity at 370 nm exhibited a progressive enhancement with increasing CA19-9 concentrations. Quantitative analysis revealed a robust linear correlation between the absorbance signal and the logarithmic value of CA19-9 concentration spanning from 2.5 to 45 U/mL. The corresponding calibration curve was y = 0.1669logC (U/mL) + 0.24644 (R^2 = 0.991, n = 21). Based on the signal-to-noise criterion (S/N = 3), the limit of detection (LOD) was 0.108 U/mL (Fig. 3E).

Preferred position of Fig. 3

Specificity, interference, repeatability, and stability

To evaluate the assay's selectivity, we challenged the sensor with a panel of physiologically relevant interferents commonly found in serum, including Ca^{2+} (1 mM), glucose (Glu, 1 mM), K^+ (1 mM), along with non-target tumor markers CEA and PCT (both at 0.1 ng/mL). As illustrated in Fig. 4A, only the target analyte CA19-9 elicited a pronounced absorbance signal, whereas the interfering species yielded responses statistically indistinguishable from the blank control. Furthermore, the coexistence of these substances with CA19-9 induced no significant deviation in signal intensity compared to CA19-9 alone (Fig. 4B), confirming that the assay is robust against potential matrix interference.

To analyze the repeatability and stability of the colorimetric immunosensor, five sets of colorimetric immunosensors were concurrently constructed under identical conditions. As depicted in Fig. 4C and D, CA19-9 detection was performed using sensors sourced from the same and different batches. The resulting intra-assay and inter-assay CVs were 2.78% and 4.62%, underscoring the high degree of precision and consistency of the method. Hence, the developed colorimetric immunosensor demonstrates favorable repeatability and stability.

Preferred position of Fig. 4

Detection of real serum samples

Clinical feasibility of the developed colorimetric immunoassay was evaluated using human serum specimens procured from the First Hospital of Shanxi Medical University. Method validation was

performed by statistically comparing assay outcomes against standard clinical laboratory results. As summarized in Table 1, the calculated t_{exp} values for all tested samples were consistently lower than the two-tailed critical threshold (t_{crit} = 4.303), indicating statistical congruence between the two datasets. These findings substantiate the precision and robustness of the proposed sensor for quantifying CA19-9 in complex biological matrices, highlighting its translational potential for early tumor surveillance and routine clinical diagnostics.

Table 1
Comparison of the assay results for real serum samples by using the developed colorimetric immunoassay and ELISA method.

ample	Colorimetric immunoassay (X ± SD, n = 3, U/mL)	Actual value (U/mL)	t_{exp}
1	3.483 ± 13.224	3.19	1.101
2	4.925 ± 9.425	4.48	1.661
3	7.654 ± 18.172	8.77	-1.389
4	12.97 ± 9.723	11.01	2.692
5	15.163 ± 11.709	16.31	-1.119
6	20.002 ± 8.807	20.49	-0.479
7	27.895 ± 7.375	26.68	1.023
8	32.327 ± 6.891	30.27	1.6
9	37.153 ± 13.172	41.58	-1.567

Preferred position of Table 1

Conclusion

In summary, we have engineered a photo-activated colorimetric immunosensor utilizing a CdS/Ag_2S/g-C_3N_4 ternary heterojunction for the ultrasensitive quantification of the tumor biomarker CA19-9 in serum. The rational design of this Type-II heterojunction broadens the light-harvesting spectrum and promotes efficient charge carrier separation. Consequently, the nanocomposite exhibits robust peroxidase-like activity under visible light, catalyzing the oxidation of TMB without the need for exogenous H_2O_2. By replacing the conventional enzyme-H_2O_2 system with a light-driven catalytic process, the platform mitigates the inherent instability of peroxide substrates and prevents the photodegradation of biomolecules, thereby significantly improving assay robustness and biocompatibility. Validation against clinical serum specimens demonstrated a strong correlation with standard clinical assays, underscoring the platform's potential for reliable diagnostic applications. In the future, more tumor markers can be detected by replacing the corresponding antibodies.

Declarations

Author contributions Yan Cheng and Bing Zhang provided the experimental plan and wrote the main manuscript text. Pengcheng Zhang and Shicheng Chen collected blood samples and tested biosensor. Huiling Xue and Ying Zhan built the biosensor.

Funding This research was funded by the Natural Science Foundation of Shanxi Province (No. 20210302123142).

Data availability Data will be made available on request..

Competing interests The authors declare no competing interests.

Ethical approval Blood samples were collected from First Hospital of Shanxi Medical University accordance with the guidelines approved by the First Hospital of Shanxi Medical University ethical committee (ID: IIT-2025-047).

References

1. Shen Y, Liu M, Xu M, Xu Z, Na Y, Zhang N, Geng F (2019) Simultaneous determination of nine trace concentration angiotensin peptides in human serum using ultra high performance liquid chromatography with tandem mass spectrometry with sephadex LH-20 gel solid-phase extraction. J Sep Sci 42(13):2247–2254. https://doi.org/10.1002/jssc.201801276
2. Pendry S D, Singhal N, Neo E L, Foreman D, Winter J M (2024) Elevation of the tumor marker CA19-9 in a pancreatic cancer survivor with benign prostatic hyperplasia: a clinical case report. Clin Case Rep 12(6):e8929. https://doi.org/10.1002/ccr3.8929
3. Masuda T, Beppu T, Miyata T, Okabe H, Imai K, Sakamoto K, Miyamoto Y, Hayashi H (2026) Prognostic role of CA19-9 in patients undergoing hepatectomy for colorectal liver metastases. Cancers 18(10):1624. https://doi.org/10.3390/cancers18101624
4. Liu H N, Yao C, Wang X F, Zhang N P, Chen Y J, Pan D, Zhao G P, Shen X Z, Wu H, Liu T T (2023) Diagnostic and economic value of carcinoembryonic antigen, carbohydrate antigen 19 – 9, and carbohydrate antigen 72 – 4 in gastrointestinal cancers. World J Gastroenterol 29(4):706–730. https://doi.org/10.3748/wjg.v29.i4.706
5. Kim H M, Kim M J, Sung W, Youn Y, Park J, Hwang J H, Lee J C, Yoon S, Park J H, Lee S K (2026) Sensitive fiber-optic localized surface plasmon resonance sensor for early pancreatic cancer detection via carbohydrate antigen 19 – 9 and supplementary biomarkers. Talanta 299:129133. https://doi.org/10.1016/j.talanta.2025.129133
6. Anger F, Lock J F, Klein I, Hartlapp I, Wiegering A, Germer C T, Kunzmann V, Löb S (2022) Does concurrent cholestasis alter the prognostic value of preoperatively elevated CA19-9 serum levels in patients with pancreatic head adenocarcinoma? Ann Surg Oncol 29(13):8523–8533. https://doi.org/10.1245/s10434-022-12581-2

7. Muratore S, Zeng X, Korc M, McElyea S, Wilhelm J, Bellin M, Beilman G (2016) Metastatic pancreatic adenocarcinoma after total pancreatectomy islet autotransplantation for chronic pancreatitis. Am J Transplant 16(9):2747–2752. https://doi.org/10.1111/ajt.13851
8. Deng X, Qin X, Luo Z, Hu S, Li J, Deng B (2026) Band engineering of Cu-doped carbon quantum dot/FeOOH Z-type heterojunction for enhanced electrochemiluminescent detection of carbohydrate antigen 19 – 9. Talanta 309:130044. https://doi.org/10.1016/j.talanta.2026.130044
9. Zheng D (2025) Highly sensitive photoelectrochemical sensor for carbohydrate antigen 19 – 9 detection based on cauliflower heterostructure of NiS@Ni_3S_2/RGO/CdS composite. Inorg Chem Commun 178(Part 1):114513. https://doi.org/10.1016/j.inoche.2025.114513
10. Oliveira D, Oliveira P, Xu A, Rodrigues E, Guerreiro S G, Castro R C, Ribeiro D S M, Santos J L M, Piloto A M L (2025) Optical immunosensor panel using quantum dot–antibody conjugates for highly sensitive detection of carbohydrate antigen 19–9 (CA19-9). Anal Chim Acta 1333:343399. https://doi.org/10.1016/j.aca.2024.343399
11. Luo N, Wang Y, Zhou M, Zhang J, Li J, Wang Y, Zhang J, Cheng Y (2026) Dopamine-mediated signal amplification integrated with CCK-8 detection for highly sensitive colorimetric immunoassay. Spectrochim Acta A 360:128042. https://doi.org/10.1016/j.saa.2026.128042
12. Zhang R, Chen X, Deng X, Pan Y, Lin Y, Tang D, Lai W (2026) A FeS_2@NiS nanozyme-based colorimetric immunoassay for sensitive detection of carcinoembryonic antigen. Microchem J 221:117088. https://doi.org/10.1016/j.microc.2026.117088
13. Yu Z, Xu M, Xu M, Gu J, Xue H, Tang D (2026) Fe–N_3S single-atom nanozyme with asymmetric coordination for ultra-low-background colorimetric immunoassays. Anal Chem 98(2):1783–1792. https://doi.org/10.1021/acs.analchem.5c07715
14. Ecke A, Bell J, Schneider R J (2023) A three-dimensional microfluidic flow cell and system integration for improved electrochemical substrate detection in HRP/TMB-based immunoassays. Sensors Diagn 2(4):887–892. https://doi.org/10.1039/D3SD00095H
15. Khramtsov P, Novokshonova A, Galaeva Z, Morozova M, Bezukladnikova T, Rayev M (2025) A systematic investigation of TMB substrate composition for signal enhancement in ELISA. Anal Biochem 704:115908. https://doi.org/10.1016/j.ab.2025.115908
16. Lei J, Nong H, Meng F, Huang L, Tan H (2026) Photoactive nanomaterials for mitigating food risk factors: advances, mechanisms, and future perspectives. J Agric Food Chem 74(5):4249–4272. https://doi.org/10.1021/acs.jafc.5c14486
17. Chen K, Loynachan C N, Thanapongpibul C, Zhang J, Ma L, Yeow J, Najer A, Stevens M M (2025) Photo-PISA driven in situ encapsulation of nanocluster-based sensors within stimuli-responsive polymersomes for AND logic gate sensing. ACS Sens 10(11):8778–8789. https://doi.org/10.1021/acssensors.5c02685
18. Qin J, Li J, Zeng H, Du F, Tang D, Tang J (2023) Bifunctional TiO_2 nanoflower-induced H_4TCBPE aggregation enhanced electrochemiluminescence for an ultrasensitive assay of organophosphorus. Anal Chem 95(48):17903–17911. https://doi.org/10.1021/acs.analchem.3c04183

19. Li J, Xiong P, Tang J, Liu L, Gao S, Zeng Z, Xie H, Tang D, Zhuang J (2021) Biocatalysis-induced formation of BiOBr/Bi_2S_3 semiconductor heterostructures: a highly efficient strategy for establishing sensitive photoelectrochemical sensing system for organophosphorus pesticide detection. Sens Actuators B 331:129451. https://doi.org/10.1016/j.snb.2021.129451
20. Chen Y, Hu T, Ai J, Zhou Q, Su X, Zhang Y, Zhang H, Guan S, Bian Z, Yamashita H (2026) Targeted O_2 activation over cyano-functionalized g-C_3N_4 enhances visible-light photocatalytic dissolution of precious metals. ACS ES&T Eng 6(5):1682–1690. https://doi.org/10.1021/acsestengg.6c00236
21. Zhao Y, Zhang H T, Wan-Me Z X, Wen H Z, Wan X Y, Xie Y L, Pan L (2025) Molten-salt-engineered graphitic C_3N_4/$ZnIn_2S_4$ composites for accelerated charge separation in photocatalytic hydrogen production. ACS Appl Nano Mater 8(40):19619–19629. https://doi.org/10.1021/acsanm.5c03679
22. Zhurenok A V, Tkachenko P A, Ermoshkina A E, Mishchenko D D, Aydakov E E, Gerasimov E E, Kozlova E A (2026) Effect of Ni loading on the structure and photocatalytic performance of g-C_3N_4-based photocatalysts. Inorg Chem Commun 188:116505. https://doi.org/10.1016/j.inoche.2026.116505
23. Jiang R B, Yu F C, Duan X Y, Zhang J L, Ren J L, Yu X H, Liu L N, Feng C C, Li C X, Hu K C, Hou X G (2025) Study on heterojunctions-based g-C_3N_4/ZnCdS/MoO_3 composite photocatalyst with a dual S-scheme carrier transfer mechanism. J Alloys Compd 1037:182394. https://doi.org/10.1016/j.jallcom.2025.182394
24. Xu Y R, Zhang H F, Zhang Z L, Li J, Zong F F, Qi Y R, Wang Y R, Wu Y D (2026) Novel Dual Type-II WO_3/g-C_3N_4/Cu_2O-Au Heterojunction-Based Photoelectrochemical Aptasensor for Ultra-Sensitive AFB_1 Detection in Astragalus Matrix. Microchim Acta 193(1):35. https://doi.org/10.1007/s00604-025-07752-3
25. Du Q Y, Zhang H Y, Bi Y N, Wang H J, Zhou X M, Shi P F, Lv S Z, Bi S (2025) N-Deficient B-Doped g-C_3N_4/CdS Heterojunction-Based PEC-FL Biosensor Assisted by CRISPR-Cas12a System for Ultrasensitive Determination of microRNA. Anal Chem 97(7):4049–4056. https://doi.org/10.1021/acs.analchem.4c05841
26. Tang J, Xiong P, Cheng Y, Chen Y, Peng S, Zhu Z Q (2019) Enzymatic Oxidate-Triggered AgNPs Etching: A Novel Signal-On Photoelectrochemical Immunosensing Platform Based on Ag@AgCl Nanocubes Loaded RGO Plasmonic Heterostructure. Biosens Bioelectron 130:125–131. https://doi.org/10.1016/j.bios.2019.01.014

Schemes

Scheme 1 is available in the Supplementary Files section

Figures

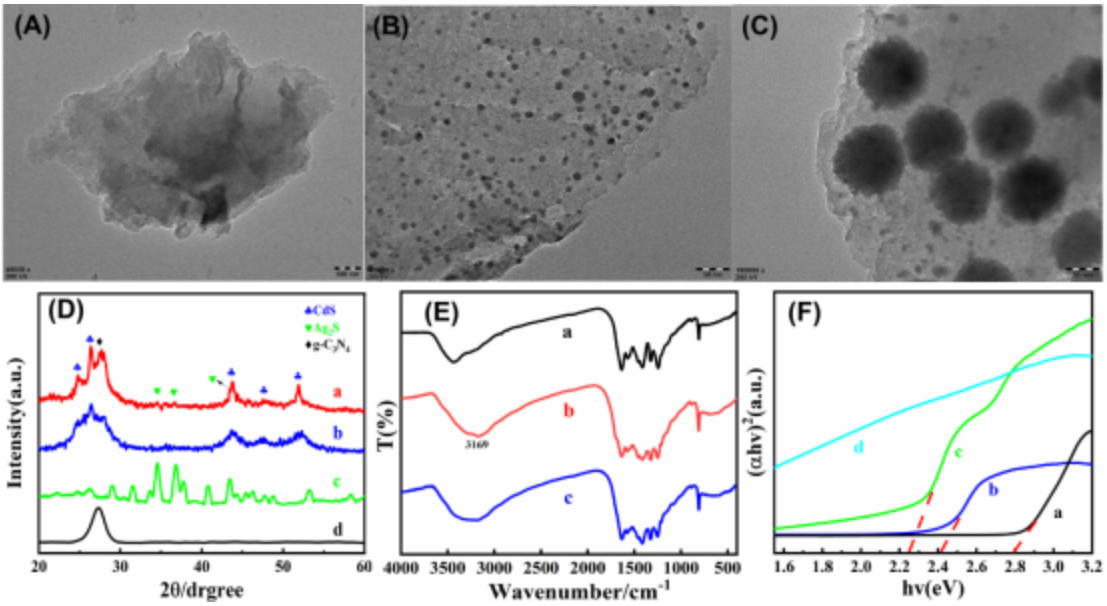


Figure 1

TEM of (A) g-C_3N_4, (B) Ag_2S/g-C_3N_4, and (C) CdS/Ag_2S/g-C_3N_4; (D) XRD of (a) CdS/Ag_2S/g-C_3N_4, (b) CdS, (c) Ag_2S, and (d)g-C_3N_4; (E) FTIR of (a) g-C_3N_4, (b) carboxylated g-C_3N_4, and (c) CdS/Ag_2S/g-C_3N_4; (F) T_{auc} of (a) g-C_3N_4, (b) CdS, (c) Ag_2S, and (d) CdS/Ag_2S/g-C_3N_4.

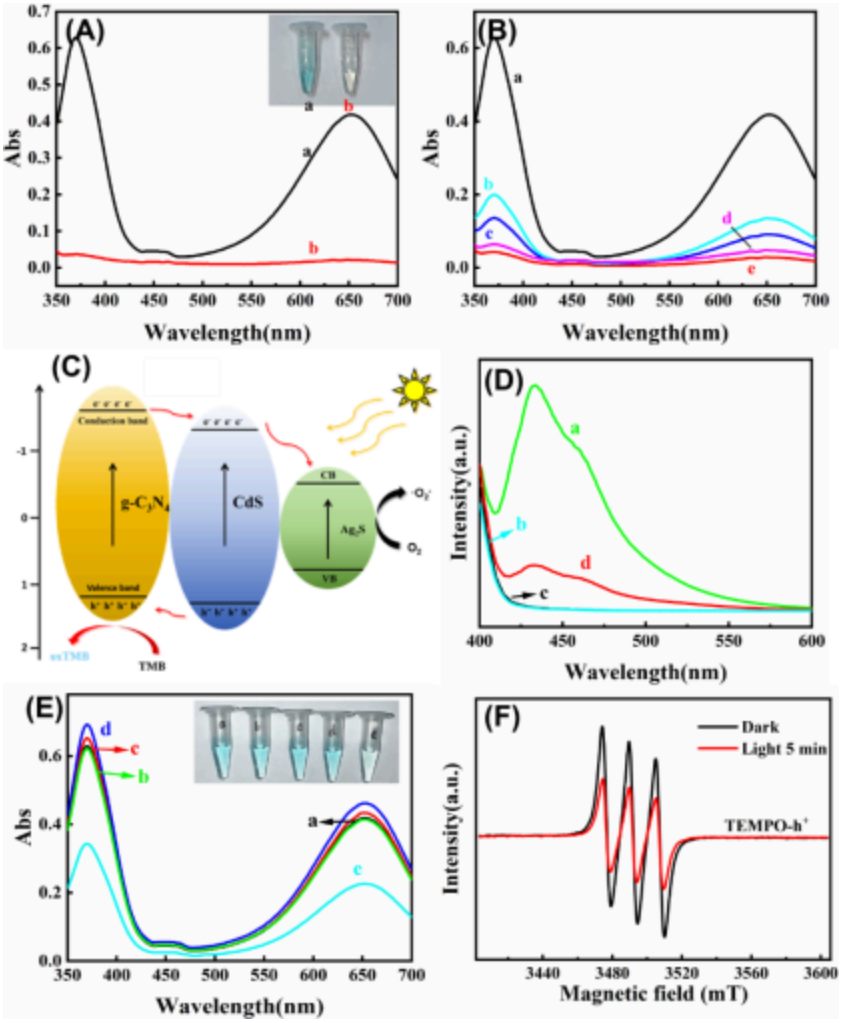


Figure 2

(A) UV-vis spectrum of $CdS/Ag_2S/g\text{-}C_3N_4$ system under (a) light and (b) dark conditions; (B) UV-vis spectrum under visible light irradiation of (a) TMB + $CdS/Ag_2S/g\text{-}C_3N_4$, (b) TMB + CdS, (c) TMB + $g\text{-}C_3N_4$, (d) TMB + Ag_2S, and (e) TMB; (C) Schematic diagram of electron transfer mechanism in the $CdS/Ag_2S/g\text{-}C_3N_4$ heterojunction for catalyzing TMB oxidation under visible light; (D) PL of (a) $g\text{-}C_3N_4$, (b) CdS, (c) Ag_2S, and (d) $CdS/Ag_2S/g\text{-}C_3N_4$; (E) UV-vis spectrum after addition of different scavengers under visible-light irradiation; (F) EPR spectrum of TEMPO-h^+.

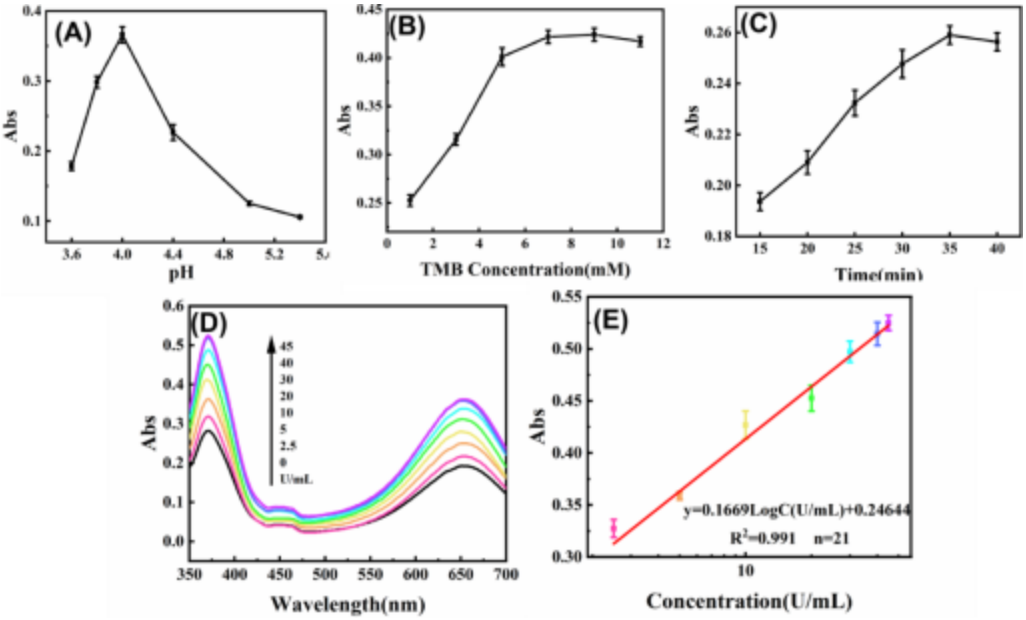


Figure 3

The effect of (A) pH; (B) concentration of TMB; and (C) incubation time of antigen-antibody; (D) UV-vis spectrum toward different concentrations of CA19-9; (E) Calibration plots of the colorimetric immunoassay toward different concentrations of CA19-9.

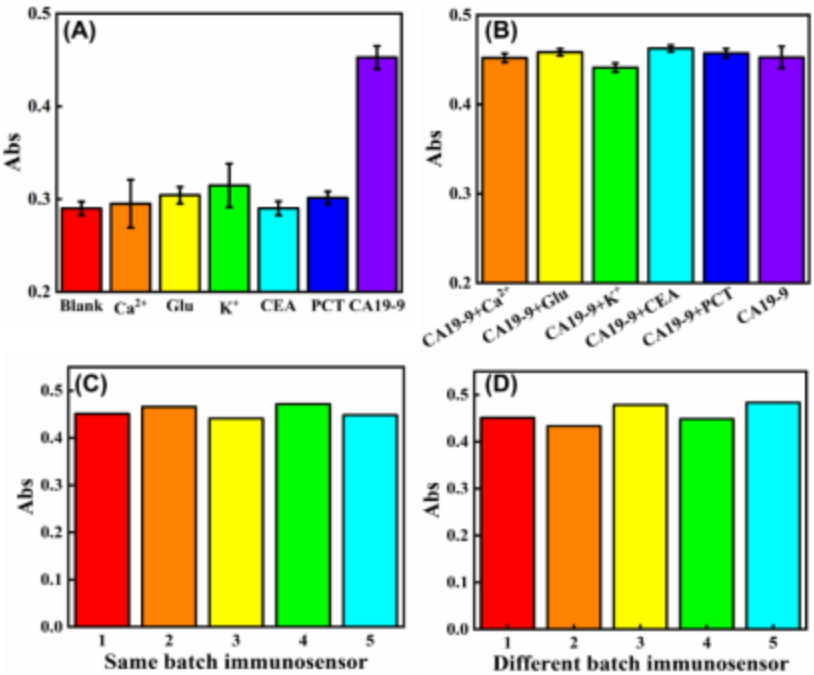


Figure 4

(A) Selectivity and (B) anti-interference of colorimetric immunoassay; Stability of colorimetric immunosensors with (C) same batch and (D) different batch.

Supplementary Files

This is a list of supplementary files associated with this preprint. Click to download.

- GraphicalAbstract.tif
- floatimage1.png